

Atomic layer deposition of ferroelectric $\text{Hf}_{0.5}\text{Zr}_{0.5}\text{O}_2$ on single-layer, CVD-grown graphene

Suzanne Lancaster, Iciar Arnay, Ruben Guerrero, Adrian Gudín, Alejandra Guedeja-Marrón, Jose Manuel Diez Toledano, Jan Gärtner, Alberto Anadón, Maria Varela, Julio Camarero, Thomas Mikolajick, Paolo Perna & Stefan Slesazeck

February 28, 2022

Dr. S. Lancaster, J. Gärtner, Prof. T. Mikolajick, Dr. S. Slesazeck
NaMLab gGmbH, Nöthnitzer Str. 64a, 01187 Dresden, Germany
Email Address: suzanne.lancaster@namlab.com

Dr. I. Arnay, Dr. R. Guerrero, A. Gudín, Dr. Alberto Anadón, Dr. P. Perna
IMDEA Nanociencia, c/ Faraday 9, 28049 Madrid, Spain
A. Guedeja-Marrón, Prof. M. Varela
Departamento de Física de Materiales and Instituto Pluridisciplinar, Universidad Complutense de Madrid, Ciudad Universitaria, 28040 Madrid, Spain.

J. M. Díez Toledano, Prof. Julio Camarero
IMDEA Nanociencia, c/ Faraday 9, 28049 Madrid, Spain.
Departamento de Física de la Materia Condensada & Departamento de Física Aplicada & Instituto Nicolás Cabrera, Universidad Autónoma de Madrid, 28049 Madrid, Spain.

Prof. T. Mikolajick
IHM, TU Dresden, Nöthnitzer Str. 64, 01187 Dresden, Germany

Abstract

Although technologically challenging, the integration of ferroelectric thin films with graphene spintronics potentially allows the realization of highly efficient, electrically tuneable, non-volatile memories. Here, the atomic layer deposition (ALD) of ferroelectric $\text{Hf}_{0.5}\text{Zr}_{0.5}\text{O}_2$ (HZO) directly on graphene (Gr)/Co/heavy metal (HM) epitaxial stacks is investigated via the implementation of several nucleation methods. With an in-situ method employing an Al_2O_3 layer, the HZO demonstrates a remanent polarization ($2Pr$) of $19.2 \mu\text{C}/\text{cm}^2$. An ex-situ, naturally oxidized sputtered Ta layer for nucleation produces a film with $2Pr$ of $10.81 \mu\text{C}/\text{cm}^2$, but a lower coercive field over the stack and switching enduring over subsequent cycles. Magnetic hysteresis measurements taken before and after ALD deposition show strong perpendicular magnetic anisotropy (PMA), with only slight deviations in the magnetic coercive fields due to the HZO deposition process, thus pointing to a good preservation of the single-layer Gr. X-ray diffraction measurements further confirm that the high-quality interfaces demonstrated in the stack remain unperturbed by the ferroelectric deposition and anneal.

1 Introduction

Graphene, besides being considered as a candidate for traditional electronics [1], has recently found applications in emerging fields such as spintronic devices [2, 3], offering long spin lifetimes and long spin propagation lengths [4]. While graphene exhibits negligible intrinsic spin-orbit coupling (SOC), it can be amplified

by a proximity effect [5], for example when integrated with a heavier atom [6, 7, 8]. In addition, it has been shown that the graphene-ferromagnet interface enhances interfacial perpendicular magnetic anisotropy (PMA) [9, 10] in Co/heavy metal (HM) stacks. This improvement is generated by the enhancement of orbital magnetic moment anisotropy promoted by the presence of Gr through the hybridization between the π -band of Gr with the 3d-orbital of Co [10, 11], extending the Co thickness range for exhibiting PMA up to 4 nm. Further, such Gr/Co interfaces present sizeable Dzyaloshinskii-Moriya interaction (DMI) [12, 10], which is critical for stabilizing skyrmionic spin textures [13] being particularly interesting in the case of graphene [14], as the interfacial magnetic interactions may be efficiently electrically tuned.

At the same time, the recent discovery of ferroelectricity in doped HfO_2 thin films [15] has opened up a new avenue for ferroelectric research, with many benefits compared to classic perovskite materials [16]. Perovskite films are typically ~ 70 nm thick, compared to ~ 5 -20 nm for hafnia ferroelectrics, which limits device scaling. Further, HfO_2 -based ferroelectrics profit from CMOS-compatibility [17]. This offers new opportunities for the integration of ferroelectric films in non-volatile memory devices such as capacitor-based random access memories, ferroelectric field-effect transistors and ferroelectric tunnel junctions [18, 19, 20, 21].

Bringing these two breakthroughs together, the integration of ferroelectric thin films on graphene could further enable the use of graphene in non-volatile memories [22, 23], as well as opening up opportunities for the non-volatile control of graphene's SOC-mediating properties, amongst other applications. To-date, the integration of ferroelectrics on graphene is sparse, mostly focusing on spin-coated polymers [24] or the exfoliation of graphene onto perovskite substrates [25] or, most recently, ferroelectric HZO thin films [26]. For the chemical vapour deposition (CVD) of graphene, where large-scale, single-layer graphene (SLG) can be reliably deposited on various metal substrates [27], subsequent transfer of the film can lead to a deterioration in material quality [28], while also losing any scaling benefits and the precise control over interface properties. In this paper, we demonstrate the direct integration of a $\text{Hf}_{0.5}\text{Zr}_{0.5}\text{O}_2$ (HZO) ferroelectric thin film onto CVD-grown graphene via atomic layer deposition (ALD). This finding opens up new possibilities for the engineering of layer stacks containing graphene, while maintaining the advantages of large (mm)-scale integration and a high material quality.

2 In-situ methods for nucleation on the graphene surface

2.1 Film deposition and characterization

Some studies in literature have focused on the deposition of various dielectric materials on graphene (Gr) and other 2D materials, as summarized in reference [29]. The deposition depends sensitively on surface functionalization, precursor and oxidant choice, and temperature.

HZO films discussed here were deposited with HyALD and ZyALD as Hf and Zr precursor, respectively. These precursors cannot be used with H_2O as an oxidant, which has been shown to have good wetting of Gr at lower temperatures, so that physisorption can be used in the absence of chemisorption to promote film growth [30]. Of the remaining oxidants, O_3 , while demonstrated to functionalize the Gr surface at room temperature, is damaging to SLG at elevated temperatures such as those required for ferroelectric deposition [31]. Furthermore, the choice of oxidant has been shown to limit the temperature range in which the ferroelectric orthorhombic phase can be formed [32], and for applications in spin-orbitronics which exploit interfacial effects, lower temperatures are needed to prohibit intermixing of Co and Pt [33]. Therefore, a method was developed using a remote O_2 plasma as an oxidant, with the plasma source located around 30 cm from the substrate. Under these conditions, the damage to SLG should be minimised [34].

Figure 1 shows the results of an atomic force microscopy (AFM) and grazing incidence X-ray diffraction (GIXRD) study on in-situ nucleation methods on the Gr surface of Gr/Pt(111) stacks, with a Pt thickness of 30 nm. An AFM map of the pristine Gr surface before any deposition is shown in figure 1a. For the

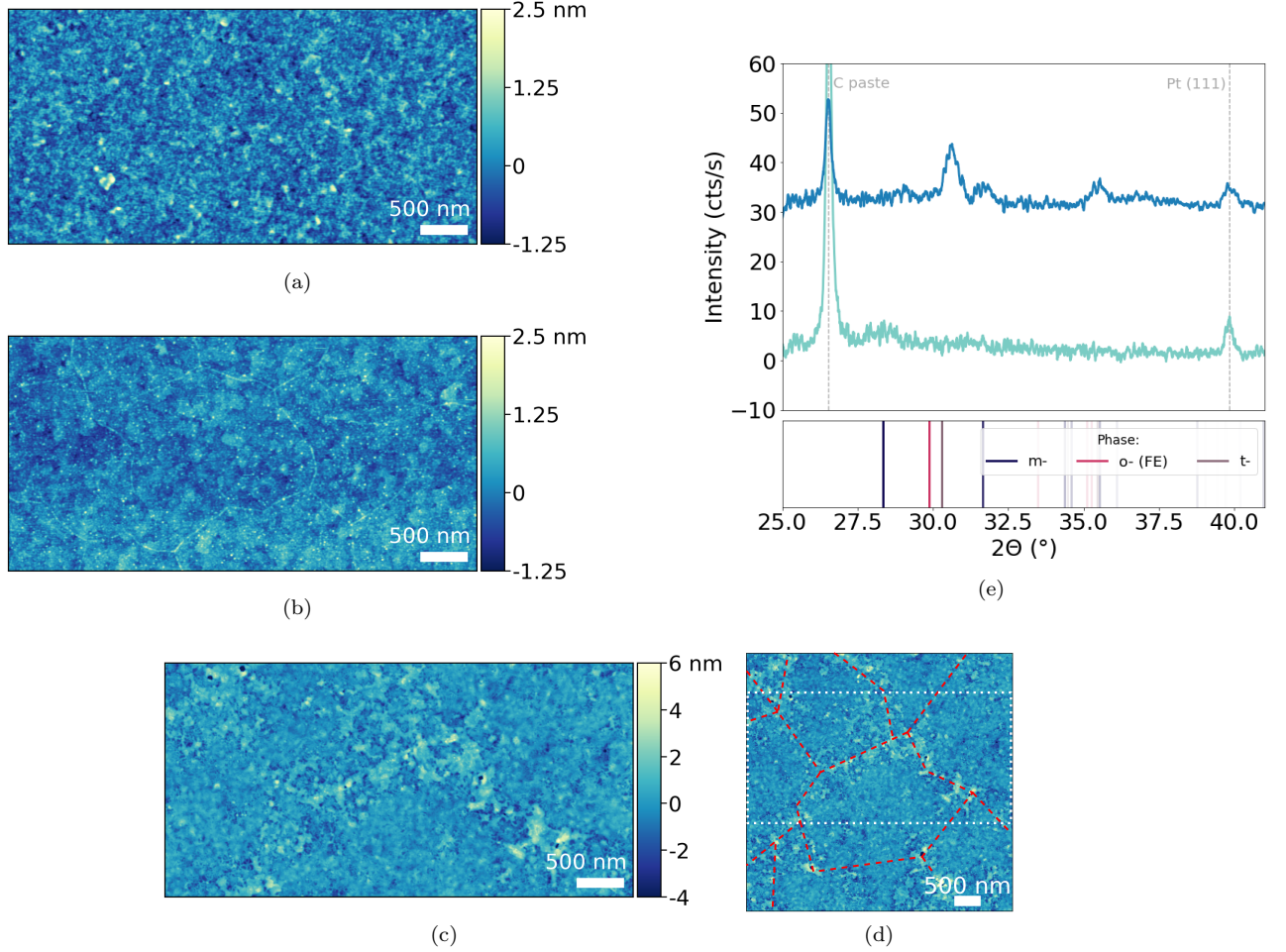


Figure 1: AFM study of in-situ nucleation steps: (a) pristine Gr surface before any nucleation; (b) after three extended cycles HyALD with O_2 as oxidant and 110 cycles of HZO deposition; (c) after 3 cycles TMA with H_2O as oxidant; (d) full AFM map from (c) (the white dotted lines indicate the reduced area) with probable step edges marked with red dashed lines. (e) GIXRD scans of HZO films deposited after 3 cycles (green) and 6 cycles (blue) of Al_2O_3 deposition.

first three deposition cycles the HyALD precursor residence time was increased to promote chemisorption, followed by deposition of HZO and finally Al_2O_3 (full details are given in methods). A subsequent AFM map was recorded and is shown in figure 1b. While no conformal film was deposited, decorated lines appear, indicating enhanced reactivity at some sites on the Gr surface. The size of these features, (1-2 μm), is consistent with step edges previously observed in scanning tunneling microscopy (STM) experiments on similar films [33]. Depending on the ALD precursor used, the energy barrier for chemisorption is increased [35] and thus nucleation may be favoured only at more reactive sites, such as these step edges. The roughness is similar for both the pristine Gr surface and the surface in 1b, at around 0.35 nm, which is slightly higher than a single step edge in Pt(111), 0.238 nm [36].

In a second experiment, a seed layer of Al_2O_3 was deposited, followed by 11 nm HZO and a capping layer for crystallization. For the seed layer only, a lower growth temperature of 150°C was employed. For Al_2O_3 deposited with a trimethylaluminum (TMA) precursor, H_2O can be employed as an oxidant and deposition can occur at a reduced temperature, so that enhanced physisorption of water molecules can assist

in nucleation on the Gr surface [30]. In these samples, the metal substrate is expected to play a role in the ALD process by further increasing wetting of the surface by H_2O [37]. The lower temperature brings an additional benefit of reducing any possible damage to the underlying Gr layer.

Figure 1c shows an AFM map of the sample surface after 3 deposition cycles of the Al_2O_3 interlayer. Line defects (such as step edges) in the Gr layer also increase the wettability, which explains why there are some regions of thicker deposition, as indicated by the red dashed lines on the larger-scale image in figure 1d, which are of similar structure to the features seen in figure 1b. Furthermore, the increased average roughness of 0.69 nm reveals the improved surface coverage, pointing to a more efficient nucleation even after very few ALD cycles. The slight deviations in height appear to reduce as the film thickness increases, and are absent in scanning electron microscopy (SEM) and AFM images of the full film, as shown in supplementary figure ??, where the roughness is slightly reduced again to 0.52 nm.

In order to assess the ferroelectricity of the deposited HZO, GIXRD measurements were performed. Figure 1e shows 2θ scans for ~ 15 nm films deposited after Al_2O_3 nucleation for 3 cycles (green) and 6 cycles (blue), measured after annealing. Crystalline peaks of HZO first appear after 6 nucleation cycles, suggesting that below this, nucleation on the surface with H_2O is incomplete. After 6 cycles, crystalline peaks can be observed in the GIXRD scan, indicating the HZO is composed of a mixture of the non-ferroelectric monoclinic (m-)phase, ferroelectric orthorhombic (o-)phase and antiferroelectric tetragonal (t-)phase. The main peak in the GIXRD scan is at around 31° , which is consistent with literature values for a mixed o-/t-phase, while a significant m-phase portion is still visible at 28° and 32° .

2.2 Electrical characterization of in-situ nucleated films

After observation of the o-phase in the deposited films, electrical polarization-voltage (P-V) and current-voltage (I-V) measurements were performed for confirmation of their ferroelectricity, as presented in **figure 2**. First, capacitors were formed on the whole stack, shown schematically in figure 2a, with the Al_2O_3 capping layer intact. Capacitors were defined with diameters of 200 μm (as described in methods). The I-V (solid lines) and P-V (dashed lines) characteristics of such a device are plotted in figure 2b, measured via a dynamic hysteresis measurement (DHM) with the pulse train shown in the inset. The voltage was varied from 10-14 V. Below this voltage range, no ferroelectric switching peaks are visible, while above 14 V the sample breaks down, resulting in a large leakage.

The sample demonstrates asymmetric switching properties, with a positive/negative coercive voltage $V_c^{+/-}$ of +5.7/-7.2 V and remanent polarization $P_r^{+/-}$ of +3.1 and -3.3 $\mu\text{C}/\text{cm}^2$, respectively. The high coercive voltages are related to the Al_2O_3 layers surrounding the HZO [38]. Since the plotted voltage is applied across the whole stack (including Al_2O_3), a certain voltage is dropped across these interlayers, depending on their dielectric constant and thickness, which decreases the voltage drop across the FE layer and thus increases the apparent coercive voltage extracted from I-V and P-V curves. Further, the imprint observed (shift to negative voltages along the stack) indicates an internal bias field in the sample, which can be related to fixed charges generated during annealing [39], either in the interfacial layers or the HZO, as well as the inherent asymmetry caused by the fabrication flow of the sample.

To confirm this, the top Al_2O_3 layer was etched away and additional top electrodes deposited on the same sample, as shown schematically in 2c. When the same DHM experiment is repeated (figure 2d), the coercive voltage is reduced to $V_c^{+/-} = +2.7/-4.5$ V and the remanent polarization increased to $P_r^{+/-} = +10.3/-8.9$ $\mu\text{C}/\text{cm}^2$. These improvements can be directly linked to the removal of one interfacial layer, with a reduced depolarization field leading to a higher P_r and a larger voltage drop across the ferroelectric producing a lower apparent V_c . The imprint effect remains, which hints towards vacancies created within the HZO layer itself, likely due to oxygen scavenging from the top and/or bottom Al_2O_3 layers, as the main cause of the observed internal bias field.

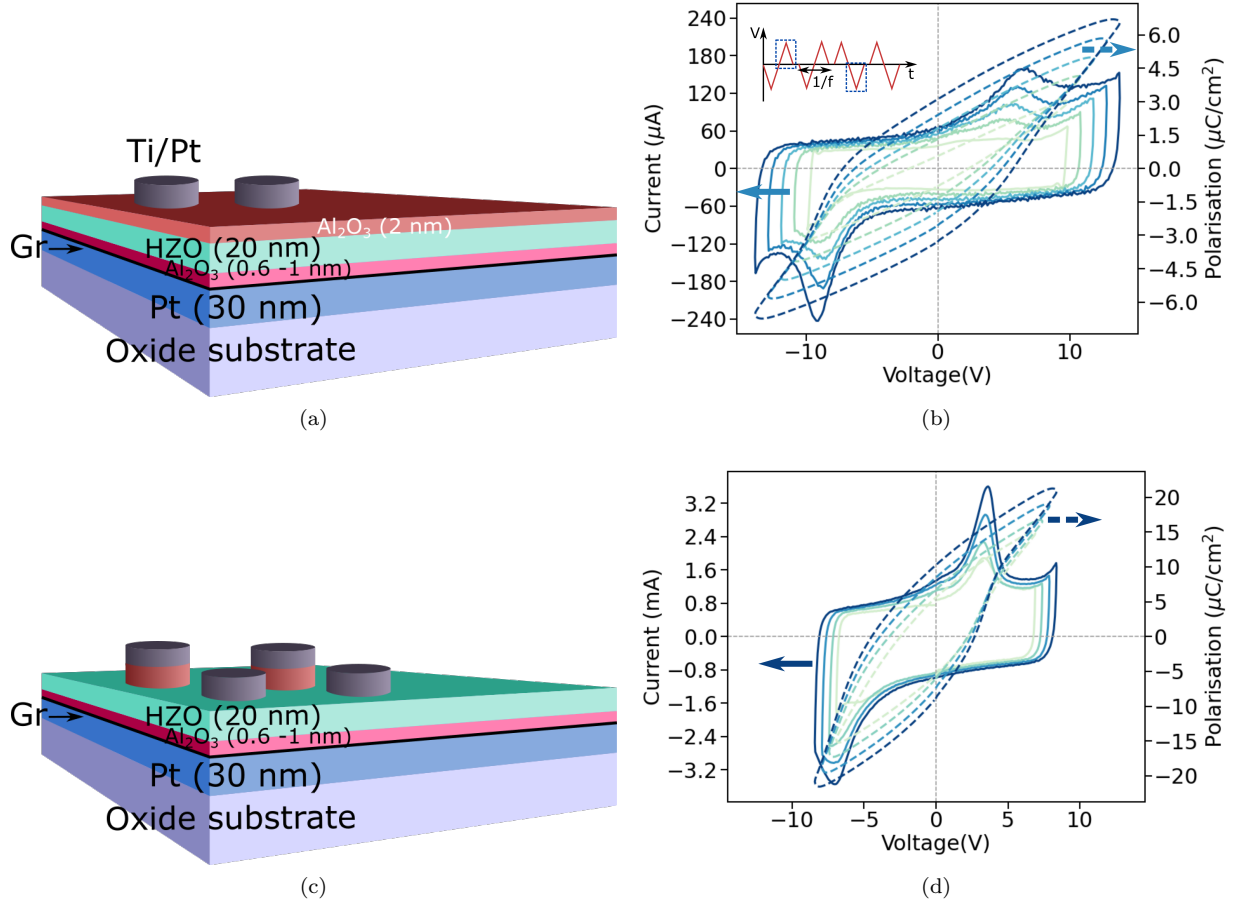


Figure 2: Electrical characterization of HZO films: (a) schematic and (b) measured switching characteristics of devices with the Al_2O_3 capping layer intact (inset: DHM pulse sequence, with blue dashed lines highlighting the pulses plotted here); (c) schematic and (d) measured switching characteristics of devices after etching away of top Al_2O_3 layer

Finally, the experiment described here was repeated on a sample with a lower HZO thickness (10 nm). As shown in supplementary figure ??, this leads to an expected increase in remanent polarization to $P_r^{+/-} = +7.77/-7.89 \mu\text{C}/\text{cm}^2$. However, the devices broke down at 10 V before full switching could occur, so that V_c could not be properly estimated.

In both cases, the devices broke down after a single switching cycle, and some were shorted even during the first measurement. This fast breakdown is attributed to pinholes in the nucleation layer (figure 1c) which can propagate through the HZO and cause shorts. Such pinholes were observed in SEM images of the final samples, as shown in supplementary figure ??. This presents a clear need for the improvement of the film quality. One possibility is increasing the conformality of the Al_2O_3 layer by careful control of the precursor pulse and purge times, and further reducing the deposition temperature [30]. Nonetheless, the thickness of the nucleation layer is clearly critical in increasing the device coercive voltage as well as the stability of the resulting ferroelectric state, and in general, deposition of conformal Al_2O_3 on Gr requires relatively thick oxides of several nms [40].

3 Ex-situ methods for nucleation on graphene

3.1 Film deposition and characterization

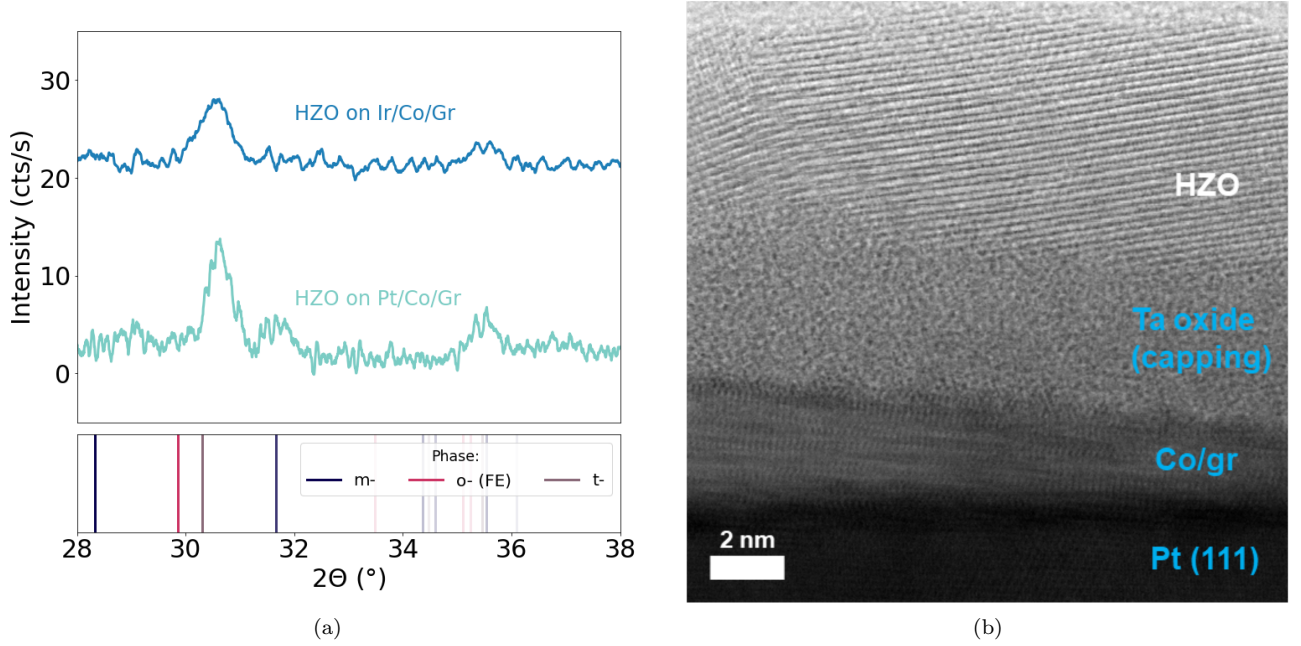


Figure 3: Structural characterization of ex-situ nucleated HZO films: (a) 2θ scans of HZO films deposited on two different stacks with Ta as a nucleation layer; (b) High resolution annular bright field STEM image of the stack deposited on Pt (111).

To that end, another approach was investigated, where the nucleation layer for HZO is an ex-situ deposited transition metal which oxidizes in atmosphere before the ALD process. For this experiment, a 2 nm layer of Ta was deposited on the Gr/Co/HM(111) [10] as described in methods. Previous transmission electron microscopy measurements, not shown, indicate that this thin layer of Ta becomes fully oxidised upon exposure to atmosphere. Then, 11 nm HZO and 2 nm Al_2O_3 were deposited and annealed as before. GIXRD and high-resolution scanning transmission electron microscopy (STEM) measurements on these samples are presented in **figure 3**.

Ferroelectric o-/t-phase peaks were observed in GIXRD scans, as shown in figure 3a. Notably, a slight reduction is seen in the non-ferroelectric monoclinic peaks at $\sim 28^\circ$ and 32° . The relative intensities of m- and o-phase are well-known to depend on the underlying substrate [41] and the corresponding strain state of the HZO layer [42].

Also visible in figure 3a is a significant shift of the HZO peaks, which indicates an altered strain state in films deposited on stacks with a different heavy metal element (blue: Ir/ green: Pt). These observations demonstrate that the underlying substrate is providing the template for the crystal properties of deposited HZO. Thus, having careful control over the metallic stack supporting the Gr allows us to tune both the

ferroelectric properties and quality of the deposited HZO.

A high-resolution annular bright field STEM image of the stack deposited onto Pt(111) is represented in figure 3b. The HZO layer is polycrystalline, while the Ta oxide capping layer appears amorphous. Low magnification images (not shown) exhibit continuous layers over long lateral distances, with relatively even thicknesses. No major interfacial intermixing due to the processing of the FE layer can be detected from these images. This was verified on a larger scale, as demonstrated in figure ??, and the chemical composition of the films was measured with electron energy-loss spectroscopy (EELS, figure ??), further confirming that the deposition method leaves the underlying stack intact.

3.2 Electrical characterization of ex-situ nucleated films

Capacitor structures were defined as for the previous samples, directly on samples with the Al_2O_3 capping layer etched away. Electrical characterization of these capacitors are presented in **figure 4**. Switching peaks were observed at a much lower maximum applied voltage V_{max} of <5 V, as shown in the switching IV curves shown in 4a. In these measurements, a significant leakage current was observed, particularly at $V_{max} = 5$ V. One cause of this leakage current could be a scavenging of oxygen from the HZO by the underlying sub-stoichiometric TaOx layer.

Endurance measurements, that is switching measurements with intermediate cycling, were performed at 4.5 V and a measurement frequency of 1 kHz, to avoid early breakdown of the devices due to leakage and high switching currents. Cycling was performed with square pulses at 100 kHz. For these measurements, a PUND (positive up, negative down) pulse train, as shown inset in figure 4b, was applied. This method allows us to separate switching from non-switching contributions to the current, i.e. the dielectric displacement current and the significant leakage observed previously.

As can be seen from figures 4b & (c), capacitors display ferroelectric behavior with $P_r^{+/-}$ up to $+6.44/-4.37$ $\mu\text{C}/\text{cm}^2$ and $V_c^{+/-}$ of $+2.02/-1.87$ V. The films endure up to 10^4 switching cycles at 4.5 V before breakdown, however, the switching current is seen to reduce over time. The decrease of ferroelectricity with cycling, known as fatigue, is common in all HZO films, but is pronounced in these devices, with the switching completely lost after about 50 switching cycles. This corresponds with a shift in V_c to more negative voltages, i.e. a negative imprint. The presence of imprint as the film fatigues hints that the reduction in ferroelectricity is linked to the redistribution of charges within the layer stack and subsequent domain pinning [43]. Further, looking at the negative switching curves in figures 4a and 4b, the hysteresis may not be fully saturated at the applied field. Larger fields are above the dielectric breakdown of the film. In order to attain an improved endurance, both the interlayer properties and HZO film quality should be improved, to reduce internal fields, increase the breakdown strength and avoid pinning of domains by charged defects. One significant source of charged defects could be the aforementioned oxygen scavenging of the nucleation layer.

4 Post-deposition sample characterization

4.1 X-ray characterization of metallic stacks

Figure 5 shows the X-ray analysis of the film stacks before and after HZO deposition. In panel a, X-ray reflectivity (XRR) measurements show the appearance of well-defined intensity oscillations due to the interference between reflected x-rays at the different interfaces of the heterostructure, demonstrating the presence of abrupt interfaces, also after HZO deposition. Besides the $\text{Al}_2\text{O}_3[0006]$ crystallographic reflection from the substrate (at $2\theta = 41.7^\circ$), $\theta - 2\theta$ diffraction patterns in panel b recorded in the heterostructures present an intense peak centered at $2\theta = 39.8^\circ$, which corresponds with Pt[111]. Despite the reduced Co thickness, we could observe a further peak at $2\theta = 44.2^\circ$ due to the relaxed out-of-plane $\text{Co}_{fcc}[111]$. Panel c presents

the rocking curves around the Pt[111] reflection proving that HZO deposition does not induce additional structural disorder in the Pt structure. In summary, the XRD measurements demonstrate the epitaxial growth of the Pt and Co layers, which grow (111)-oriented on top of the Al₂O₃ (0001) substrate. After HZO deposition, contributions from Pt and Co remain unchanged, indicating the preservation of the structural properties of the stack after the ALD process.

4.2 Magnetic hysteresis measurements on HM/FM/Gr/HZO stacks

The magnetic properties of the samples were ex-situ investigated at RT by means of magneto-optical Kerr effect (MOKE) magnetometry in polar geometry. In precedent works, we have demonstrated that on both Pt and Ir HM buffers, the samples present a well-defined PMA for Co layer thinner than 4 and 2 nm for Pt and Ir buffers, respectively. In this range of thicknesses, the hysteresis present sharp transitions and a remanence magnetization (i.e., at zero field) almost 100% of the magnetization saturation value (M_S , i.e. at field larger than the anisotropy field), as well as large coercive fields. By combining Kerr, X-ray magnetic circular dichroism, high-resolution transmission electron microscopy and ab-initio modelling, we previously ascribed such behavior to a large magnetic anisotropy due to the anisotropy of the orbital moment, which is of interfacial nature [11].

Figure 6 shows the out-of-plane magnetization component M_z normalized to the saturation value M_S as a function of the applied perpendicular magnetic field $\mu_0 H_z$ acquired in several samples, before and after the ALD deposition of the ferroelectric HZO layer. The measurements demonstrate that the samples possess PMA both without (blue filled squares) and with (empty black circles) the HZO layer, presenting sharp and abrupt magnetization reversals, large coercive field, and fully remanence magnetization state. The cycles before and after the HZO deposition in the stacks with Pt-buffers in figure 6a and 6b) are similar and do not present relevant differences, indicating that the Gr stays intact during the ALD deposition and thus the expected PMA enhancement at the Gr/Co interface is observed, along with the expected dependence on Co thickness.

Nonetheless, in the case of Gr/Co/Ir(111) (figure ?? in Supp. Info.), we notice a slight increase of coercive field after the ALD deposition of the HZO, which is probably due either to a minor partial oxidation of Co (this may be due to some damage of the underlying Gr layer) or Co/HM intermixing (this may be favored by the elevated deposition temperature used for the ALD growth and subsequent annealing, to be further investigated). This effect is greatly reduced in Gr/Co/Pt(111) samples (figure 6a and 6b). In any case, the strong similarity in PMA before and after deposition indicates that these are both minor effects, which do not substantially affect the overall magnetization reversals behavior of the Gr/Co system.

5 Conclusion

Deposition of ferroelectric HZO on graphene was demonstrated utilizing both an in-situ and an ex-situ nucleation layer method. The optimised in-situ method employed 6 cycles of a low-temperature Al₂O₃ film deposited with H₂O as an oxidant, providing good wetting of the graphene layer which enabled subsequent film deposition. However, high coercive voltages and low endurance were attributed to pinholes in the film. An ex-situ deposited Ta film, oxidised in atmosphere, provides uniform coverage and an adequately reactive surface for the deposition of HZO. In this case, the films could be switched at < 5 V, with $2P_r$ values of ~ 11 $\mu\text{C}/\text{cm}^2$, and the films could be switched for several cycles, although the polarization decreased with cycling.

Through utilizing a substrate which exhibits interfacial perpendicular magnetic anisotropy in contact with graphene, magnetic hysteresis measurements allowed us to characterize this effect both before and after the ALD deposition of HZO. Both curves showed sharp magnetization reversals and large (~ 50 -75 mT) magnetic coercive fields, with the coercive field after deposition increasing slightly due to intermixing effects which occurs during the HZO deposition and anneal. This proves that the ALD process leaves the Gr layer intact, and demonstrates the possibility of applying this process in spin-orbitronics applications combining

ferromagnetic and ferroelectric materials.

These first results open up pathways for investigating the integration of HZO and other HfO_2 -based ferroelectrics directly on graphene. Through careful tuning of the interlayer properties and ALD deposition parameters, the ferroelectric film properties such as remanent polarization and endurance can be further improved. Combined with recent advances in the CVD growth of graphene on insulating substrates [44] or on semiconductor materials such as Ge [45], this could enable the transfer-free processing of graphene as a channel material in non-volatile memories and various spintronic devices. Finally, depositing the interlayer atop graphene via physical deposition makes this method versatile for different substrates, whereby the ferroelectric properties can also be tuned depending on the supporting stack.

6 Experimental Section

6.0.1 Chemical Vapor Deposition of Graphene on Pt(111)

To obtain high-quality epitaxial Gr we utilized a chemical vapor deposition (CVD) method in ultra-high-vacuum (UHV) condition [33]. In contrast to exfoliation methods, we followed a UHV growth and in-situ characterization procedure, enabling the electronic and chemical control of the Gr interfaces while avoiding contamination, which are known to affect the overall transport properties. The fabrication of the samples was monitored by in-situ surface analysis at each stage of the growth, which consisted first in the deposition of 10 nm-thick, epitaxial, single-crystal, heavy-metal buffer (i.e., Pt(111) or Ir(111)) by dc sputtering at 550 K onto commercial $\text{SrTiO}_3(111)$ single crystal substrates. The HM buffers present a crystal quality equivalent to Pt(111) and Ir(111) single crystals, as verified by x-ray diffraction measurements (not shown here).

Then, epitaxial monolayer graphene was grown in-situ by ethylene chemical vapour deposition at 1025 K on top of the buffers. In the case of the Pt(111) buffer, the LEED and STM analyses indicate the presence of multi-domain Gr flakes (i.e., domains oriented $\pm 15^\circ$). Instead, Gr grown on the Ir(111) buffers presents the well-known “10x10” moiré pattern that is due to the incommensurate unit cells of Ir and Gr. The difference between the two cases is mostly related to the different interaction of Gr with the two heavy metals, Gr-Ir being the more intense. The details of the growth and characterization of the epitaxial stacks are reported in [33]. The epitaxial Gr/HM(111) onto $\text{SrTiO}_3(111)$ systems are then used for the ferromagnetic Co layer intercalation, as discussed in the following section.

6.0.2 HM/Co/Graphene/Ta stack deposition

To incorporate a ferromagnetic layer into the epitaxial system described above, we resorted to the thermally activated intercalation method as reported in [33]. In brief, Co was evaporated on top of Gr by molecular beam epitaxy (MBE) at RT with a deposition rate of 0.3 \AA/s monitored by an in situ quartz balance. Then, in order to favor the penetration of Co atoms underneath the Gr layer, a low-temperature anneal was applied to activate the intercalation process. Surface microscopy and in-situ spectroscopy experiments revealed that the intercalated Co is pseudomorphic with the metallic substrates, epitaxial and (111)-oriented, as well as homogeneous (over $\sim \mu\text{m}^2$) underneath Gr. In addition, these studies demonstrated that i) the Gr efficiently protected the Co from oxidation, and ii) at annealing temperature higher than 600 and 650 K for Pt and Ir respectively Co/HM intermixing occurs.

Finally, for some samples, we deposited by in-situ dc sputtering at RT 2 nm thick Ta layer on top of the final structure in order to investigate the HZO layer nucleation on Gr and to protect the underlying Co from oxidation.

6.0.3 Atomic Layer Deposition of $\text{Hf}_{0.5}\text{Zr}_{0.5}\text{O}_2/\text{Al}_2\text{O}_3$

Films were deposited in an Oxford OpAL ALD system. First, where applicable, Al_2O_3 as a nucleation layer was deposited at 150°C with TMA as the precursor and H_2O as the oxidant. Next, the temperature was ramped up to 250°C , for deposition of the HZO and subsequent Al_2O_3 , with HyALD/ZyALD/TMA as the Hf, Zr and Al precursors, respectively. For HZO films, the oxidant used was a remote O_2 plasma, at a power of 300 W and with the source located ~ 30 cm from the substrate; for Al_2O_3 , H_2O was employed as the oxidant. The HZO films were deposited at a layer ratio of 1:1 with an approximate growth rate of $1 \text{ \AA}/\text{cycle}$. HyALD and ZyALD pulse times were 2s, increased to 3s during the first nucleation experiment. The HZO thickness was varied by changing the number of cycles, while the Al_2O_3 capping layer for crystallization was kept constant at a nominal thickness of 2 nm.

Samples were annealed for 5 s at 600°C in an AST SHS-2800 RTP under N_2 atmosphere for crystallization of the HZO.

6.0.4 Atomic Force Microscopy measurements

AFM was performed in atmosphere on a Bruker Dimension XR microscope in tapping mode, with a Nanosensors Point-Probe PPP-NCHR tip of 7 nm radius.

6.0.5 X-Ray Diffraction measurements

For GIXRD, 2θ scans were measured in a Bruker D8 Discover XRD system with a Cu K- $\alpha 1$ X-ray source, a Göbel mirror and 0.2 mm divergence slit on the primary side, and a 2.5° Soller slit on the secondary side. The source was set to an angle $\Omega = 0.45^\circ$ to the sample surface.

X-Ray Reflectivity (XRR), X-ray diffraction (XRD) $\theta-2\theta$ measurements and rocking-scans were performed in a parallel beam geometry by using a commercial Rigaku SmartLab SE multipurpose diffractometer equipped with a Cu K- α source ($\lambda = 0.154\text{nm}$), a cross beam optics system and a D/Tex Ultra 250 1D silicon strip detector. The measurements were performed with a 2.5° Soller slit and a 2 mm length limit slit at the primary side and a second 2.5° Soller slit at the secondary side.

6.0.6 Capacitor fabrication

10 nm Ti and 25 nm Pt were deposited via e-beam evaporation under high vacuum through a shadow mask to form dots for the capacitors. Capacitors were either deposited on the Al_2O_3 layer, or directly to the HZO by first etching the samples for 90 s in AZ 300 MIF developer at room temperature before metallization.

6.0.7 Electrical characterization

DHM measurements were performed on an Aixacct TF3000 ferroelectric prober, at a frequency of 10 kHz.

IV switching and PUND measurements were performed using PMUs controlled by Keithley 4225 RPMs on a Keithley 4200 semiconductor probe station. The frequency for both switching and PUND measurements was 1 kHz, and no time delay was applied between subsequent PUND pulses. In endurance measurements, the device was cycled with square pulses at 100 kHz.

6.0.8 Scanning transmission electron microscopy and electron energy-loss spectroscopy

Electron microscopy observations were carried out in a JEOL ARM200cF microscope equipped with a CEOS spherical aberration corrector and a Gatan Quantum EEL spectrometer at the Centro Nacional de Microscopía Electrónica (CNME) at the University Complutense of Madrid. Specimens were prepared by conventional methods, including mechanical polishing and Ar ion milling.

6.0.9 Polar Kerr Magnetic hysteresis measurements

The RT vectorial-Kerr experiments were performed in polar configuration by using p-polarized light (with 632 nm wavelength) focused on the sample surface and analyzing the two orthogonal components of the reflected light as function of the magnetic field applied along the sample out-of-plane (\hat{z}) direction. This enables the acquisition of the hysteresis loops of the out-of-plane magnetization components, M_Z , which has been normalized to the magnetization saturation M_S .

Supporting Information

Supporting Information is available from the Wiley Online Library or from the author.

Acknowledgements

The authors would like to acknowledge fruitful discussions with Vincent Cros, Pierre Seneor and Nicolas Reyren from CNRS-Thales.

This project has received funding from the FLAG-ERA JTC 2019 grant SOgraphMEM through the partner's national research agencies AEI (Spain, PCI2019-111867-2) and DFG (Germany, MI 1247/18-1). IMDEA team acknowledges support by the Community of Madrid (CM) through Project P2018/NMT-4321 (NANOMAGCOST), by MINECO through Projects RTI2018-097895-B-C42 and RTI2018-097895-B-C43 (FUN-SOC), and by the 'Severo Ochoa' Programme for Centres of Excellence in R&D, MINECO grant SEV-2016-0686. AG and IA acknowledge support from CM (PEJD-2017-PREIND-4690 and PEJD-2019-POST/IND-15343) and JMD from MINECO (BES 2017-080617).

References

- [1] K. S. Novoselov, V. Fal, L. Colombo, P. Gellert, M. Schwab, K. Kim, et al., *nature* **2012**, *490*, 7419 192.
- [2] S. Roche, J. Åkerman, B. Beschoten, J.-C. Charlier, M. Chshiev, S. P. Dash, B. Dlubak, J. Fabian, A. Fert, M. Guimarães, et al., *2D Materials* **2015**, *2*, 3 030202.
- [3] M. Piquemal-Banci, R. Galceran, S. M.-M. Dubois, V. Zatzko, M. Galbiati, F. Godel, M.-B. Martin, R. S. Weatherup, F. Petroff, A. Fert, et al., *Nature Communications* **2020**, *11*, 1 1.
- [4] W. Han, R. K. Kawakami, M. Gmitra, J. Fabian, *Nature nanotechnology* **2014**, *9*, 10 794.
- [5] A. Avsar, J. Y. Tan, T. Taychatanapat, J. Balakrishnan, G. Koon, Y. Yeo, J. Lahiri, A. Carvalho, A. Rodin, E. O'Farrell, et al., *Nature communications* **2014**, *5*, 1 1.
- [6] D. Marchenko, A. Varykhalov, M. Scholz, G. Bihlmayer, E. Rashba, A. Rybkin, A. Shikin, O. Rader, *Nature communications* **2012**, *3*, 1 1.
- [7] F. Calleja, H. Ochoa, M. Garnica, S. Barja, J. J. Navarro, A. Black, M. M. Otrokov, E. V. Chulkov, A. Arnau, A. L. V. De Parga, et al., *Nature Physics* **2015**, *11*, 1 43.
- [8] I. I. Klimovskikh, M. M. Otrokov, V. Y. Voroshnin, D. Sostina, L. Petaccia, G. Di Santo, S. Thakur, E. V. Chulkov, A. M. Shikin, *ACS nano* **2017**, *11*, 1 368.
- [9] N. Rougemaille, A. N'Diaye, J. Coraux, C. Vo-Van, O. Fruchart, A. Schmid, *Applied Physics Letters* **2012**, *101*, 14 142403.
- [10] F. Ajejas, A. Gudín, R. Guerrero, A. Anadon Barcelona, J. M. Diez, L. de Melo Costa, P. Olleros, M. A. Niño, S. Pizzini, J. Vogel, et al., *Nano letters* **2018**, *18*, 9 5364.
- [11] M. Blanco-Rey, P. Perna, A. Gudin, J. M. Diez, A. Anadón, P. Olleros-Rodríguez, L. de Melo Costa, M. Valvidares, P. Gargiani, A. Guedeja-Marron, et al., *ACS Applied Nano Materials* **2021**.

- [12] H. Yang, G. Chen, A. A. Cotta, A. T. N'Diaye, S. A. Nikolaev, E. A. Soares, W. A. Macedo, K. Liu, A. K. Schmid, A. Fert, et al., *Nature materials* **2018**, *17*, 7 605.
- [13] A. Fert, V. Cros, J. Sampaio, *Nature nanotechnology* **2013**, *8*, 3 152.
- [14] P. Olleros-Rodríguez, R. Guerrero, J. Camarero, O. Chubykalo-Fesenko, P. Perna, *ACS Applied Materials & Interfaces* **2020**, *12*, 22 25419, pMID: 32401480.
- [15] T. Böske, J. Müller, D. Bräuhäus, U. Schröder, U. Böttger, *Applied Physics Letters* **2011**, *99*, 10 102903.
- [16] A. Bhalla, R. Guo, R. Roy, *Materials research innovations* **2000**, *4*, 1 3.
- [17] M. H. Park, Y. H. Lee, T. Mikolajick, U. Schroeder, C. S. Hwang, *MRS Communications* **2018**, *8*, 3 795.
- [18] D. Martin, E. Yurchuk, S. Müller, J. Müller, J. Paul, J. Sundquist, S. Slesazeck, T. Schloesser, R. van Bentum, M. Trentzsch, et al., *Solid-state electronics* **2013**, *88* 65.
- [19] S. Fujii, Y. Kamimuta, T. Ino, Y. Nakasaki, R. Takaishi, M. Saitoh, In *2016 IEEE Symposium on VLSI Technology*. IEEE, **2016** 1–2.
- [20] B. Max, M. Hoffmann, S. Slesazeck, T. Mikolajick, In *2018 48th European Solid-State Device Research Conference (ESSDERC)*. IEEE, **2018** 142–145.
- [21] E. Covi, Q. T. Duong, S. Lancaster, V. Havel, J. Coignus, J. Barbot, O. Richter, P. Klein, E. Chicca, L. Grenouillet, et al., In *2021 IEEE International Symposium on Circuits and Systems (ISCAS)*. IEEE, **2021** 1–5.
- [22] E. C. Ahn, H.-S. P. Wong, E. Pop, *Nature Reviews Materials* **2018**, *3*, 3 1.
- [23] M. Dragoman, A. Dinescu, F. Nastase, D. Dragoman, *Nanomaterials* **2020**, *10*, 7 1404.
- [24] Y. Zheng, G.-X. Ni, C.-T. Toh, C.-Y. Tan, K. Yao, B. Özyilmaz, *Physical review letters* **2010**, *105*, 16 166602.
- [25] W. Lee, O. Kahya, C. T. Toh, B. Özyilmaz, J.-H. Ahn, *Nanotechnology* **2013**, *24*, 47 475202.
- [26] M. Dragoman, M. Modreanu, I. M. Povey, A. Dinescu, D. Dragoman, A. Di Donato, E. Pavoni, M. Farina, *Nanotechnology* **2018**, *29*, 42 425204.
- [27] Y. Dedkov, E. Voloshina, *Journal of Physics: Condensed Matter* **2015**, *27*, 30 303002.
- [28] J. Kang, D. Shin, S. Bae, B. H. Hong, *Nanoscale* **2012**, *4*, 18 5527.
- [29] H. G. Kim, H.-B.-R. Lee, *Chemistry of Materials* **2017**, *29*, 9 3809.
- [30] Y. Zhang, Z. Qiu, X. Cheng, H. Xie, H. Wang, X. Xie, Y. Yu, R. Liu, *Journal of Physics D: Applied Physics* **2014**, *47*, 5 055106.
- [31] S. Jandhyala, G. Mordì, B. Lee, G. Lee, C. Floresca, P.-R. Cha, J. Ahn, R. M. Wallace, Y. J. Chabal, M. J. Kim, et al., *ACS nano* **2012**, *6*, 3 2722.
- [32] R. Alcalá, C. Richter, M. Materano, P. D. Lomenzo, C. Zhou, J. L. Jones, T. Mikolajick, U. Schroeder, *Journal of Physics D: Applied Physics* **2020**, *54*, 3 035102.
- [33] F. Ajejas, A. Anadon, A. Gudín, J. M. Díez, C. G. Ayani, P. Olleros-Rodríguez, L. de Melo Costa, C. Navío, A. Gutierrez, F. Calleja, et al., *ACS applied materials & interfaces* **2019**, *12*, 3 4088.

- [34] X. Tang, N. Reckinger, O. Poncelet, P. Louette, F. Ureña, H. Idrissi, S. Turner, D. Cabosart, J.-F. Colomer, J.-P. Raskin, et al., *Scientific reports* **2015**, 5, 1 1.
- [35] K. Kim, R. W. Johnson, J. T. Tanskanen, N. Liu, M.-G. Kim, C. Pang, C. Ahn, S. F. Bent, Z. Bao, et al., *Nature communications* **2014**, 5, 1 1.
- [36] K. Itaya, S. Sugawara, K. Sashikata, N. Furuya, *Journal of Vacuum Science & Technology A: Vacuum, Surfaces, and Films* **1990**, 8, 1 515.
- [37] B. Dlubak, P. R. Kidambi, R. S. Weatherup, S. Hofmann, J. Robertson, *Applied Physics Letters* **2012**, 100, 17 173113.
- [38] P. D. Lomenzo, S. Slesazek, M. Hoffmann, T. Mikolajick, U. Schroeder, B. Max, In *2019 19th Non-Volatile Memory Technology Symposium (NVMTS)*. IEEE, **2019** 1–8.
- [39] D. K. Simon, P. M. Jordan, T. Mikolajick, I. Dirnstorfer, *ACS applied materials & interfaces* **2015**, 7, 51 28215.
- [40] R. H. Vervuurt, B. Karasulu, M. A. Verheijen, W. E. M. Kessels, A. A. Bol, *Chemistry of Materials* **2017**, 29, 5 2090.
- [41] Y.-C. Lin, F. McGuire, A. D. Franklin, *Journal of Vacuum Science & Technology B, Nanotechnology and Microelectronics: Materials, Processing, Measurement, and Phenomena* **2018**, 36, 1 011204.
- [42] S. J. Kim, D. Narayan, J.-G. Lee, J. Mohan, J. S. Lee, J. Lee, H. S. Kim, Y.-C. Byun, A. T. Lucero, C. D. Young, et al., *Applied Physics Letters* **2017**, 111, 24 242901.
- [43] F. P. Fengler, M. Pešić, S. Starschich, T. Schneller, C. Künneth, U. Böttger, H. Mulaosmanovic, T. Schenk, M. H. Park, R. Nigon, et al., *Advanced Electronic Materials* **2017**, 3, 4 1600505.
- [44] J. Sun, Y. Zhang, Z. Liu, *ChemNanoMat* **2016**, 2, 1 9.
- [45] M. Lukosius, J. Dabrowski, J. Kitzmann, O. Fursenko, F. Akhtar, M. Lisker, G. Lippert, S. Schulze, Y. Yamamoto, M. Schubert, et al., *ACS applied materials & interfaces* **2016**, 8, 49 33786.

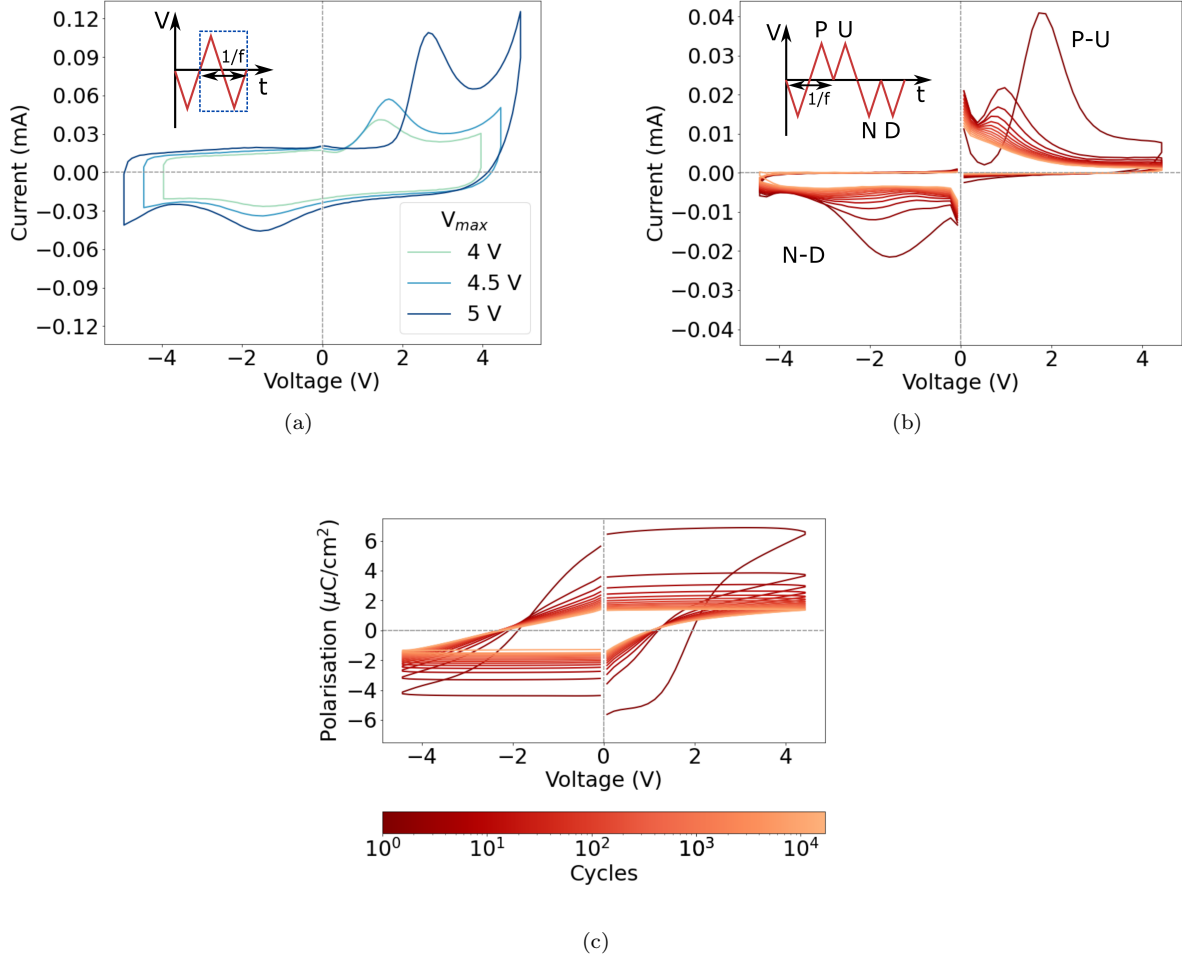


Figure 4: HZO deposition on Ta nucleation layer: (a) 2θ scans of HZO films deposited on two different stacks with Ta as a nucleation layer; (a) IV switching curves on pristine, prepoled capacitors (inset: pulse train, with blue dashed lines indicating plotted pulses) and (b) I-V and (c) P-V endurance curves extracted from PUND measurements over 10^4 switching cycles (inset: PUND pulse train), for the HZO on Pt(111)/Co/Gr sample.

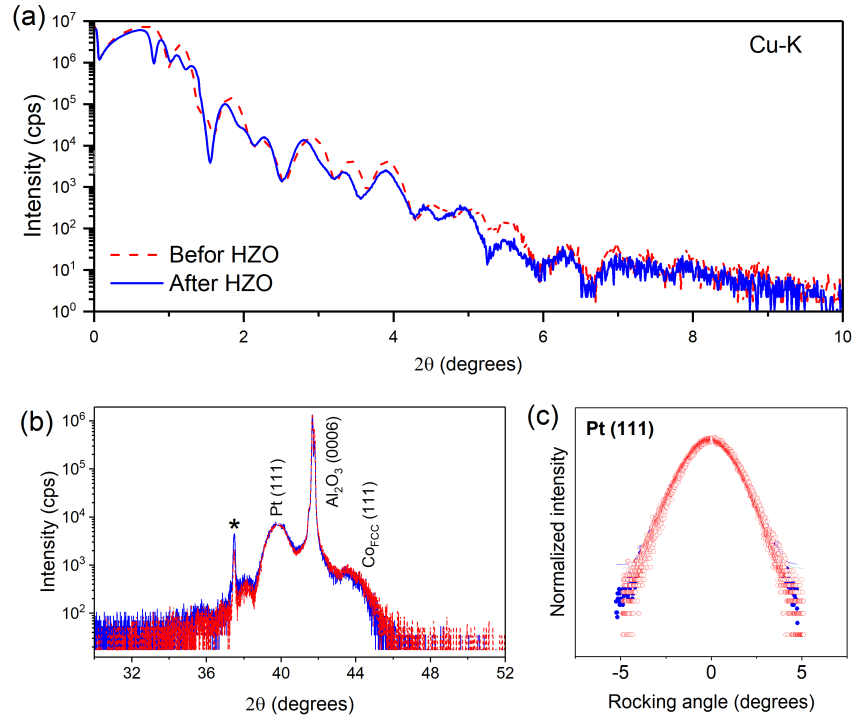


Figure 5: XRD analysis of the films before and after HZO deposition: (a) XRR measurements and (b) $\theta-2\theta$ diffraction patterns recorded in the Gr-based heterostructures before and after the HZO deposition. (c) Rocking scans around the Pt(111) reflection before and after ALD. Sharp contribution at 37.5° (*) corresponds with Al₂O₃[0006] reflection at Cu K- β energy.

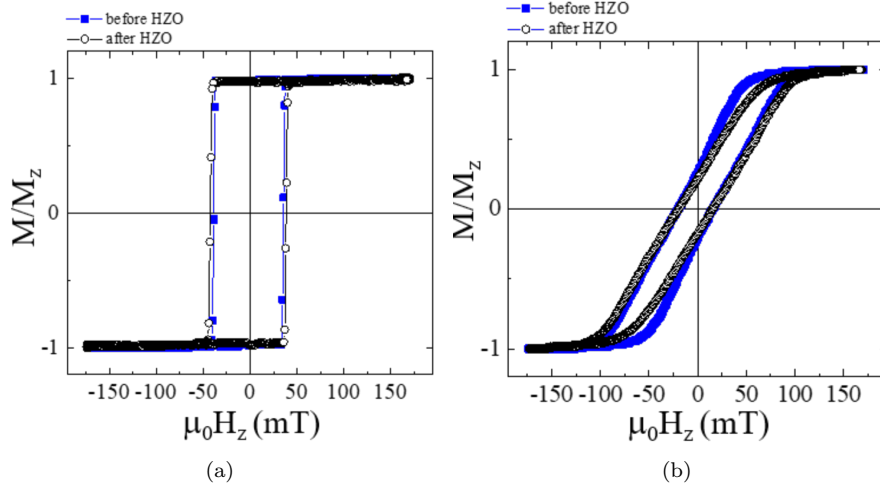


Figure 6: Magnetic hysteresis measurements on full stacks: Out-of-plane magnetization component M_z normalized to the saturation value M_S as a function of the applied perpendicular magnetic field $\mu_0 H_z$ acquired by magneto-optical (polar) Kerr magnetometry before (blue filled squares) and after (empty black circles) the ALD deposition of the ferroelectric HZO for: (a) 2 nm Co layer between Gr and Pt(111); (b) 4 nm Co layer between Gr and Pt(111)

Table of Contents

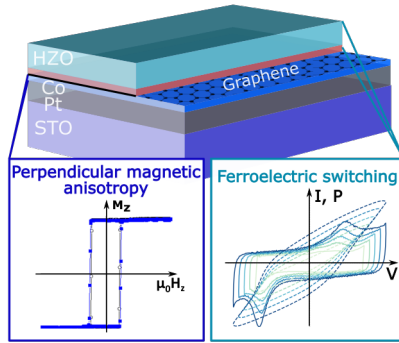
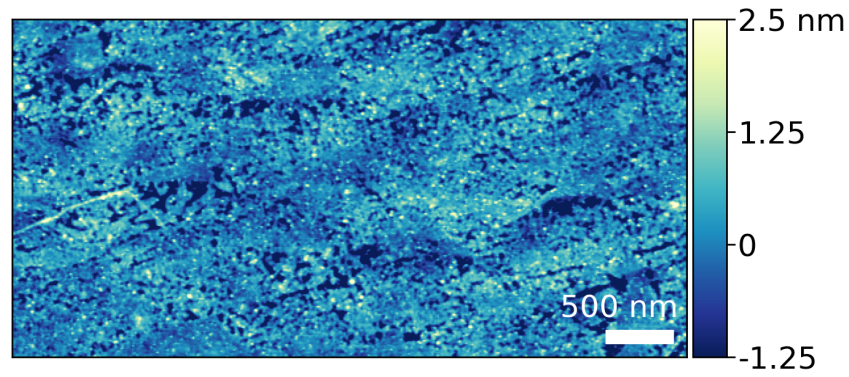


Figure 7: *

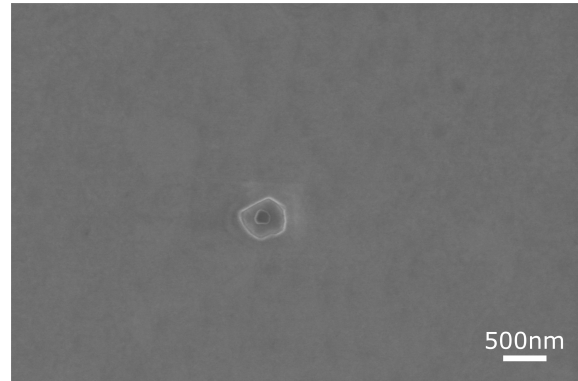
Direct integration of a $\text{Hf}_{0.5}\text{Zr}_{0.5}\text{O}_2$ layer on heavy metal/Co/single-layer graphene stacks was investigated via atomic layer deposition, utilizing different nucleation layers to enhance reactivity at the graphene surface. These films showed ferroelectric switching, while maintaining the perpendicular magnetic anisotropy of the underlying stack, indicating that the graphene and preceding interfaces stay intact and of high quality.

Atomic layer deposition of ferroelectric $\text{Hf}_{0.5}\text{Zr}_{0.5}\text{O}_2$ on single-layer, CVD-grown graphene - Supplementary Figures

February 28, 2022



(a)



(b)

Figure S1: Structural characterisation of final deposited films: (a) AFM and (b) SEM image of $\text{Hf}_{0.5}\text{Zr}_{0.5}\text{O}_2/\text{Al}_2\text{O}_3$ films after crystallisation anneal. In (b) a pinhole can be seen in the film.

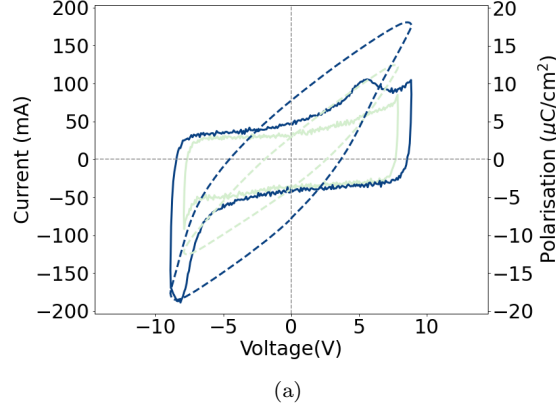


Figure S2: Electrical measurements on 10 nm HZO on an Al_2O_3 nucleation layer: Polarization-voltage and Current-voltage curves measured at $V_{max} = 8-9$ V. At 9 V, ferroelectric switching is observed. Above this, the devices break down. This can be attributed to pinholes in the nucleating Al_2O_3 layer (figure S1)

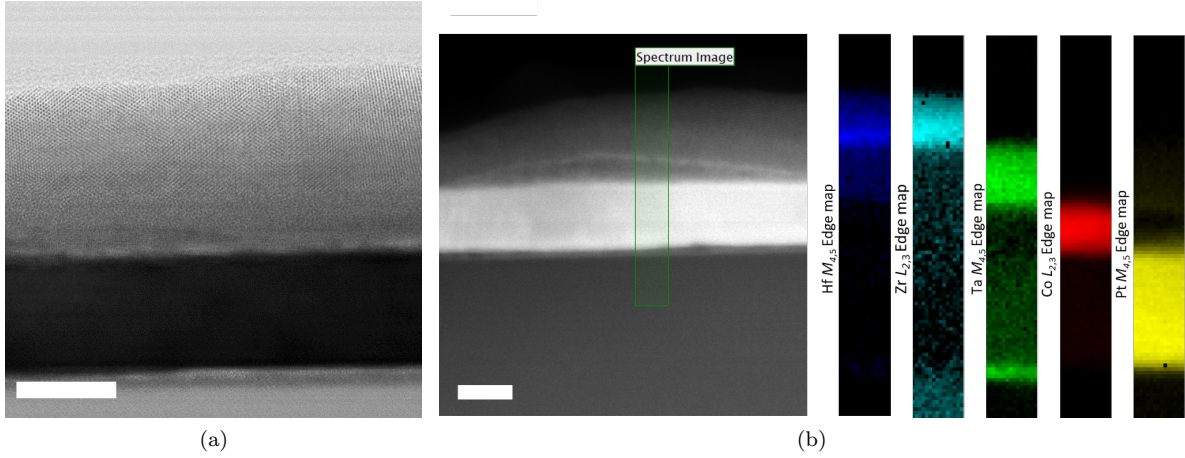
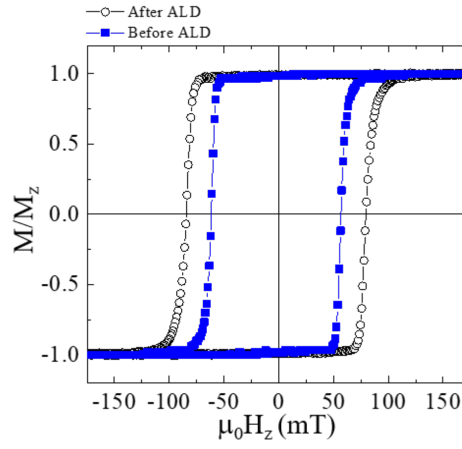


Figure S3: Cross-section STEM-EELS study of deposited films: (a) high resolution annular bright field STEM images of the full stack (HZO deposited on Pt(111)/Ta/Co/Gr), showing thickness homogeneity and the polycrystalline structure of the HZO film; (b) (Left) High angle annular dark field STEM image of the stack. A green rectangle shows the area where an EEL spectrum image was acquired. (Right) EELS maps showing the spatial distribution of the Hf, Zr, Ta, Co and Pt elemental signals, extracted from the analysis of the absorption edges marked on the panels. The scale bars represent 10 nm in all cases.



(a)

Figure S4: Magnetic hysteresis measurements on full stacks: Out-of-plane magnetization component M_z normalized to the saturation value M_S as a function of the applied perpendicular magnetic field $\mu_0 H_z$ acquired by magneto-optical (polar) Kerr magnetometry before (blue filled squares) and after (empty black circles) the ALD deposition of the ferroelectric HZO for (a) 1.5 nm Co layer sandwiched between Gr and Ir(111) buffer.